*materials*

MDPI

*Article*

# Sol-Gel Processed Cobalt-Doped Methylated Silica Membranes Calcined under $N_2$ Atmosphere: Microstructure and Hydrogen Perm-Selectivity

**Lunwei Wang [1], Jing Yang [1,*], Ruihua Mu [2], Yingming Guo [1] and Haiyun Hou [2]**

[1] School of Urban Planning and Municipal Engineering, Xi'an Polytechnic University, Xi'an 710048, China; wlw10212021@163.com (L.W.); yingming128@126.com (Y.G.)
[2] School of Environment & Chemical Engineering, Xi'an Polytechnic University, Xi'an 710048, China; 20131102@xpu.edu.cn (R.M.); houhaiyun77@126.com (H.H.)
* Correspondence: jingy76@163.com

**Abstract:** Methyl-modified, cobalt-doped silica ($Co/MSiO_2$) materials were synthesized by sol-gel technique calcined in $N_2$ atmospheres, and membranes were made thereof by coating method. The effects of Co/Si molar ratio ($n_{Co}$) on the physical-chemical constructions of $Co/MSiO_2$ materials and microstructures of $Co/MSiO_2$ membranes were systematically investigated. The gas permeance performance and hydrothermal stability of $Co/MSiO_2$ membranes were also tested. The results show that the cobalt element in $Co/MSiO_2$ material calcined at 400 °C exists not only as Si–O–Co bond but also as $Co_3O_4$ and CoO crystals. The introduction of metallic cobalt and methyl can enlarge the total pore volume and average pore size of the $SiO_2$ membrane. The activation energy ($E_a$) values of $H_2$, $CO_2$, and $N_2$ for $Co/MSiO_2$ membranes are less than those for $MSiO_2$ membranes. When operating at a pressure difference of 0.2 MPa and 200 °C compared with $MSiO_2$ membrane, the permeances of $H_2$, $CO_2$, and $N_2$ for $Co/MSiO_2$ membrane with $n_{Co}$ = 0.08 increased by 1.17, 0.70, and 0.83 times, respectively, and the perm-selectivities of $H_2/CO_2$ and $H_2/N_2$ increased by 27.66% and 18.53%, respectively. After being steamed and thermally regenerated, the change of $H_2$ permeance and $H_2$ perm-selectivities for $Co/MSiO_2$ membrane is much smaller than those for $MSiO_2$ membrane.

**Keywords:** cobalt-doped; hydrothermal stability; activation energy; $H_2$ perm-selectivities; regenerated



**Citation:** Wang, L.; Yang, J.; Mu, R.; Guo, Y.; Hou, H. Sol-Gel Processed Cobalt-Doped Methylated Silica Membranes Calcined under $N_2$ Atmosphere: Microstructure and Hydrogen Perm-Selectivity. *Materials* **2021**, *14*, 4188. https://doi.org/10.3390/ma14154188

Academic Editors: Lucjan Chmielarz, Enrica Gianotti and Ivana Miletto

Received: 1 July 2021
Accepted: 24 July 2021
Published: 27 July 2021



## 1. Introduction

Hydrogen has been recognized as an ideal energy carrier because of its clean, renewable, and high-calorific value features [1]. However, the industrially produced hydrogen from water-gas conversion process or steam reforming process [2,3] contains some other contaminants (impurities), such as $CO_2$, $N_2$, $CH_4$, CO, $H_2O$, etc. Additionally, from an environmental point of view, refining and extracting hydrogen from industrial waste gas is necessary [4]. Therefore, in order to obtain high-purity hydrogen, it is necessary to separate $H_2$ from the gas mixture. Consequently, the upgrading of hydrogen is of significant attention due to the versatile requirement for hydrogen with good purity in transportation, distributed heat, power generation, and other advanced applications [5]. Membrane separation technology has become an interesting alternative for separation and purification of hydrogen in the industry due to its energy-saving and excessive efficiency. Currently, the membranes for separating hydrogen from gas mixture mainly include inorganic membranes, such as palladium metal membranes, carbon molecular sieve membranes, and microporous ceramic membranes [6–8]. Among of them, microporous silica membranes are the most widely investigated because of their good chemical stability, large gas-permeation flux, and high selectivity.

However, pure silica membranes exhibit poor hydrothermal stability in high temperature and humid air. Because Si–O–Si linkages are damaged upon interplay with water,

Si–OH hydroxyl agencies are formed, which creates destruction and reconstruction of Si–O–Si bonds in the silica structure, resulting in densification of the silica structure [9,10]. This has been identified as a drawback in the development of silica membranes for gas separation in moist environments for practical industrial applications. An extremely good quantity of work has been done to develop and improve the stability of silica membranes under hydrothermal conditions. For one thing, the incorporation of hydrophobic groups can improve the stability of silica membranes under hydrothermal conditions, such as octyl [11], phenyl [12], alkylamine [13], methyl [14,15], perfluorodecyl [16], etc., which effectively reduce the Si–OH concentration on the surface of silica membrane materials, thereby reducing the physical adsorption of water molecules and enhancing the hydrophobicity of silica membranes. For another, further improvement of hydrothermal stability of silica membranes have been researched by introducing different types of inorganic metal/metal oxides, such as aluminum [17], zirconium [18], nickel [19,20], titanium [21], cobalt [22,23], palladium [24,25], magnesium [26], niobium [27], PdCo [28], FeCo [29], etc. They were all added in the process of sol synthesis, which produced great beneficial effects. A large number of studies have found that by introducing metal, the structure of the membrane appears to be denser, and the structural stability of the membrane material is particularly improved. This is because the mixed oxide network structure formed by incorporating transition metals is more stable than amorphous silica materials [27,30]. Among them, cobalt (Co) is an excellent dopant, and the doping of Co to $SiO_2$ matrix can reduce water adsorption, providing greater resistance by way of reducing the hydrophilicity of silica [31].

Numerous investigations have been conducted on silica materials/membranes modified by cobalt. For example, Smart et al. [32] synthesized methyl-modified $Co/SiO_2$ membranes calcined at 630 °C under air atmosphere using methyltriethoxysilane (MTES) and tetraethylorthosilicate (TEOS) as the silica source and $Co(NO_3)_2{\cdot}6H_2O$ as the cobalt source. When testing the permeability of single gas at 600 °C and a feed pressure of 600 KPa, it was observed that the $H_2$ permeation reached $1.9 \times 10^{-7}$ $mol{\cdot}m^{-2}{\cdot}Pa^{-1}{\cdot}s^{-1}$, and a $H_2/CO_2$ perm-selectivity exceeded 1500. Liu et al. [33] investigated the hydrothermal stability of the $Co/SiO_2$ xerogels calcined at 630 °C in an air atmosphere under various hydrothermal treatment conditions. For unstable xerogels (cobalt/silicon < 0.25), their stability was significantly reduced due to steam content and exposure time, leading to a surface-area reduction of nearly 90%. However, it is found that the xerogels with high cobalt content (cobalt/silicon $\geq$ 0.25) contained $Co_3O_4$ and were more stable, with a surface-area reduction of less than 25%. Esposito et al. [34] prepared cobalt-doped silica nanocomposites with various cobalt contents (cobalt/silicon = 0.111, 0.250, and 0.428) by the sol-gel process. After treatment at 400 °C under air atmosphere, the lowest cobalt-loading, cobalt-doped silica nanocomposites appeared amorphous and contained solely tetrahedral complexes of $Co^{2+}$, whilst $Co_3O_4$ was current as the solely crystalline section at greater cobalt content, besides the strong interaction of $Co^{2+}$ ions with the siloxane matrix. Many research groups found that $Co_3O_4$ was the main existing form of cobalt in the $Co/SiO_2$ material calcined under air atmosphere. However, $Co_3O_4$ is unstable in a hydrogen atmosphere and is easily reduced. According to Uhlmann et al. [35], after hydrogen reduction, the cobalt-doped xerogels calcined at 500 °C lost their crystal structure and showed no $Co_3O_4$ or CoO peaks but only a wide peak similar to that of amorphous silica. There have been a number of works revealing the effects of preparation conditions on the properties of cobalt-doped silica materials/membranes. Unfortunately, as far as we are aware, the influence of calcination atmospheres on the microstructures and characteristics of permeability for $Co/SiO_2$ membrane is crucial, but it has rarely been reported before, especially under a non-oxidizing atmosphere, such as $N_2$ atmosphere. Besides, there are few papers elaborating the influence of Co/Si molar ratio and methyl modification on the microstructures and characteristics of permeability for $Co/SiO_2$ membrane.

In this work, methyl-modified $Co/SiO_2$ ($Co/MSiO_2$) materials and membranes with different Co/Si molar ratio ($n_{Co}$) were prepared. The effect of $n_{Co}$ on the physical-chemical structures and microstructures of $Co/MSiO_2$ membrane calcined under $N_2$ atmosphere was

studied in detail. Characterization and results were attained by X-ray diffraction (XRD), X-ray photoelectron spectroscopy (XPS), Fourier transform infrared (FTIR) spectroscopy, $N_2$ sorption/desorption measurements, transmission electron microscope (TEM), and scanning electron microscope (SEM). Some gas-permeation measurements of Co/$MSiO_2$ membranes were performed and compared with each other. By observing the changes of gas-permeation characteristics before and after exposure to saturated steam, the hydrothermal stability of the Co/$MSiO_2$ membranes was additionally investigated. Subsequently, regeneration performance of the Co/$MSiO_2$ membranes for single gas was discussed.

## 2. Experimental Part

### *2.1. Fabrication of Methyl-Modified Co/$SiO_2$ Sols*

The methyl-modified Co/$SiO_2$ (Co/$MSiO_2$) sols were prepared via sol-gel process, using methyltriethoxysilane (MTES, purity 99%) and tetraethylorthosilicate (TEOS, p.a. grade) as silica sources, the cobaltous nitrate hexahydrate ($Co(NO_3)_2{\cdot}6H_2O$, purity 98%) as a cobalt source, and the nitric acid ($HNO_3$, p.a. grade) as a catalyst in conjunction with absolute ethanol (EtOH, purity 99.7%) as a solvent. The specific synthesis process is as follows: in accordance to the molar ratio of MTES:TEOS:$Co(NO_3)_2{\cdot}6H_2O$:$HNO_3$:EtOH:$H_2O$ = 0.8:1:$n_{Co}$:0.085:8.5:6.8, the required quantity of MTES, TEOS, and $Co(NO_3)_2{\cdot}6H_2O$ solution was completely dissolved in ethanol. Then, the mixed solution was placed in an ice-water bath and stirred intensely to make it fully mixed into a homogeneous solution. After the mixture solution of $H_2O$ and $HNO_3$ was poured dropwise, the reaction mixture was then stirred continuously and refluxed in a water bath at 60 °C for 180 min. Therefore, a final Co/$MSiO_2$ sol was obtained. The $n_{Co}$ is Co/Si molar ratio, which is 0, 0.08, 0.15, and 0.5, respectively.

### *2.2. Fabrication of Unsupported Co/$MSiO_2$ Materials*

The prepared Co/$MSiO_2$ sols were dried at 40 °C in a vacuum oven to prepare the dry gels. The obtained dry gels were then ground into fine powders and calcined under $N_2$ atmosphere at 400 °C in a temperature-controlled tubular furnace with the temperature rising rate of 1 °C·$min^{-1}$ for a resident time of 2 h to prepare the unsupported Co/$MSiO_2$ materials.

### *2.3. Fabrication of Supported Co/$MSiO_2$ Membranes*

To obtain the supported Co/$MSiO_2$ membranes, part of the above Co/$MSiO_2$ sols was applied to the surface of porous α-$Al_2O_3$ composite discs (Hefei Shijie Membrane Engineering Co. Ltd., Hefei, China) by dip-coating method. The discs had a thickness of 4 mm, a diameter of 20 mm, a mean pore diameter of 100 nm, and a porosity of 40%. The dipping time was 6 s. After dipping, they were dried for 3 h at 40 °C in an electric heating blast drying oven and then calcined at 400 °C under $N_2$ atmosphere in a tubular furnace for a resident time of 2 h. The process for dipping, drying, and calcination was performed once more in order to minimize any defects that might be occurred in the Co/$MSiO_2$ membrane layer. The Co/$MSiO_2$ membrane with $n_{Co}$ = 0 is also referred to as $MSiO_2$ membrane. The prepared supported $MSiO_2$ and Co/$MSiO_2$ membranes were used to test the permeances of $H_2$, $CO_2$, and $N_2$.

### *2.4. Characterization*

The material phase structure was determined by a Rigaku D/max-2550pc X-ray diffractometer (XRD, Rigaku D/max-2550pc, Hitachi, Tokyo, Japan) with CuKα radiation under the conditions of 40 kV and 40 mA. The functional groups of samples were characterized by Fourier transform infrared spectroscopy (FTIR, Nicolet 5700, Thermo Nicolet Corporation, WI, USA), and the wavelength measurement range was 400~4000 $cm^{-1}$ by KBr compression method. The chemical components of Co/$MSiO_2$ samples were performed by an X-ray photoelectron spectrometer (XPS, ESCALAB250xi, Thermo Scientific, MA, USA) with AlKα excitation. The transmission electron microscopy (TEM, JEM 2100F,

JEOL, Tokyo, Japan) was used to analyse the crystallization of the Co/$MSiO_2$ powders. The morphologies of surface and cross-sections for the membranes were observed by a scanning electron microscopy (SEM, JEOL JSM-6300, Hitachi, Tokyo, Japan) under 5 kV acceleration voltage. The BET surface area and pore volume of the samples was measured by $N_2$ sorption/desorption isotherm with a specific surface area and pore-size analyzer (ASAP 2020, Micromeritics, GA, USA).

The schematic diagram of experimental devices used to test single gas-permeation measurement is shown in Figure 1. Before testing the experiments, pressure and temperature were kept at 0.35 MPa and 200 °C for 0.5 h until gas permeation achieved a stable state. The $MSiO_2$ and Co/$MSiO_2$ membranes were tested using high-purity $H_2$, $CO_2$, and $N_2$, respectively. Additionally, the steam stability of $MSiO_2$ and Co/$MSiO_2$ membranes was examined by exposure to saturated steam at 200 °C for 10 days. After steam-stability test, the thermal regeneration of $MSiO_2$ and Co/$MSiO_2$ membranes was carried out at 350 °C with the aid of the equal calcination process as described above. The gas permeance was calculated as the usage of the outlet gas flow rate. The values of gas perm-selectivity were calculated from the ratio of individual gas-permeance values at the same transmembrane pressure difference and temperature.

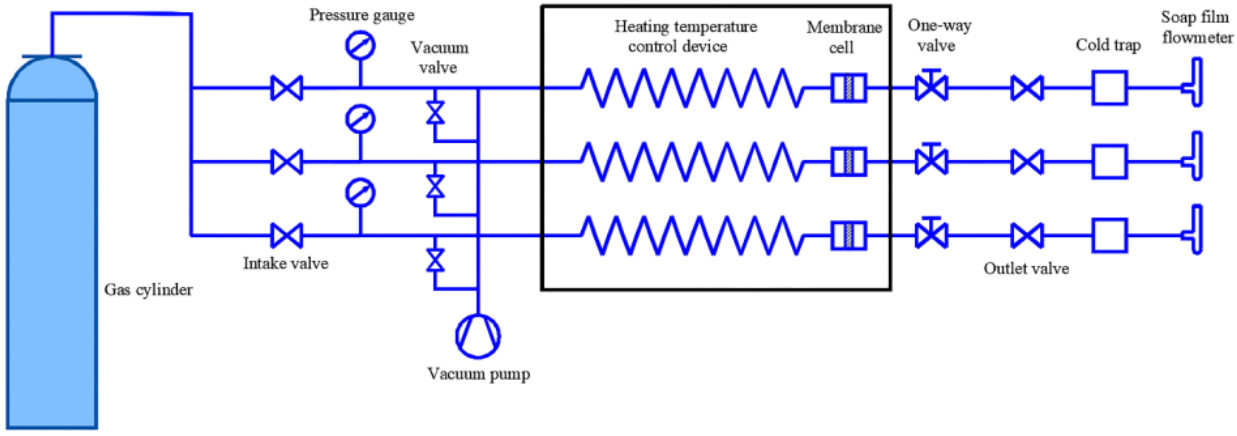


**Figure 1.** Schematic diagram of experimental devices for permeation measurement of single gas.

## 3. Results

### *3.1. Phase Structure Analysis*

The XRD patterns of the unsupported Co/$MSiO_2$ materials with various $n_{Co}$ calcined at 400 °C under $N_2$ atmosphere are provided in Figure 2. A distinct diffraction peak at about $2\theta = 23°$ is assigned to the feature of amorphous $SiO_2$ for all samples, and the peak intensity decreases with increasing $n_{Co}$. It is probably because the introduction of cobalt atoms replaces the original silicon atoms and forms the Si–O–Co bonds, resulting ultimately in an increase in Si–O–Co bonds and a decrease in $SiO_2$. When $n_{Co}$ is equal to 0.5, significant absorption peaks appeared at $2\theta = 36.57$, 42.49, 61.64, 73.86, and 77.74°, which corresponds to the plane reflections of (111), (200), (220), (311), and (222) of CoO crystalline phase (PDF No. 70-2855), respectively, which indicates part of the cobalt is dispersed on the surface of the material in the shape of CoO. There are no peaks of CoO and $Co_3O_4$ in unsupported Co/$MSiO_2$ material with $n_{Co} = 0$. However, the characteristic peak of CoO in the samples with $n_{Co} = 0.08$ and 0.15 is not obviously observed, which may be due to the fact that the CoO amount is too low or the size of the formed CoO is too small to be detected [36,37]. According to the literature, the XRD patterns of Co-doped silica powders with a cobalt mole fraction of 33% sintered at 550 °C with an existing $Co_3O_4$ peak [38]. In this paper, when $n_{Co}$ is equal to 0.08–0.5, no characteristic peak of $Co_3O_4$ is observed in the samples calcined at 400 °C, which does not mean that $Co_3O_4$ is not present

in the sample. This may be owing to the fact that the content of $Co_3O_4$ is small and cannot be detected by XRD [36].

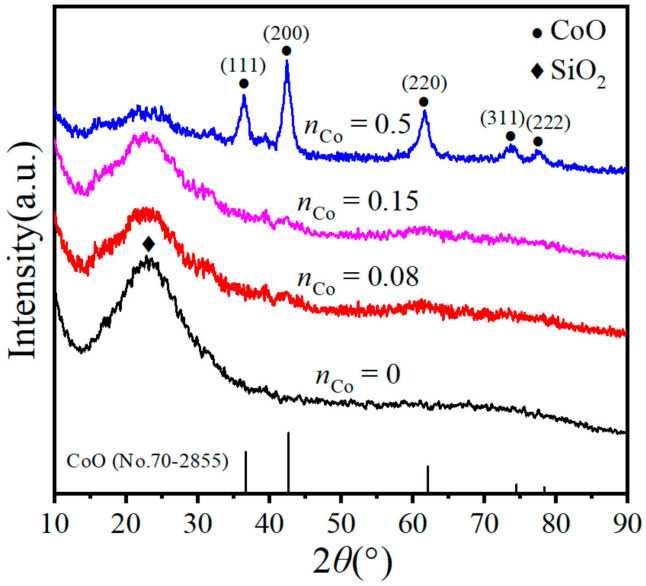


**Figure 2.** XRD patterns of unsupported Co/$MSiO_2$ materials with various $n_{Co}$ calcined at 400 °C under $N_2$ atmosphere.

The full-width at half maxima of the characteristic reflection with the highest intensity (200) was used to calculate the mean crystallite size with the aid of making use of the Scherrer equation [39]:

$$D = \frac{k\lambda}{\beta \cos\theta} \quad (1)$$

where $D$ is the size of CoO crystallites, $k$ is the constant value of Scherrer (0.89), $\lambda$ is the wavelength of X-ray source (0.154 nm), $\beta$ is the full width at half maximum intensity, and $\theta$ is the Bragg angle. Hence, the mean size of CoO crystals in the samples with $n_{Co}$ = 0.5 is calculated as 3.8 nm.

In order to further determine the presence of Co species in the unsupported Co/$MSiO_2$ materials with $n_{Co}$ = 0.08, 0.15, and 0.5 calcined at 400 °C under $N_2$ atmosphere. We characterized the unsupported Co/$MSiO_2$ material with $n_{Co}$ = 0.08 by XPS. The XPS spectra curves for samples are displayed in Figure 3. The peaks at 786.2 eV and 801.3 eV are assigned to the $2p_{3/2}$ and $2p_{1/2}$ peaks of $Co_3O_4$, respectively, and the peaks of 789.1 eV and 803.3 eV correspond to the $2p_{3/2}$ and $2p_{1/2}$ peaks of CoO, respectively [40]. Additionally, two shake-up satellite peaks can be seen at 792.8 eV and 808.3 eV, which are because of the multi-electron excitation of $Co^{2+}$ [28]. However, the binding energies of $Co_3O_4$ and CoO in the $SiO_2$ material are higher than that of the pure component, as previously reported [41]. This is resulted from the formation of the Si–O–Co bond between Co oxides and Si atoms due to the interaction of electrons. Hence, the XPS investigation clearly indicated that the doped Co component is present in the oxide rather than the metal. This result was confirmed by XRD analysis. For the samples with even higher Co content, such as unsupported Co/$MSiO_2$ materials with $n_{Co}$ = 0.15 and 0. 5, the Co signal becomes very strong (especially the latter one), and it is obvious that the peaks of $Co_3O_4$ and CoO are found in the samples by spectrum analysis. Therefore, the results are not included for comparison.

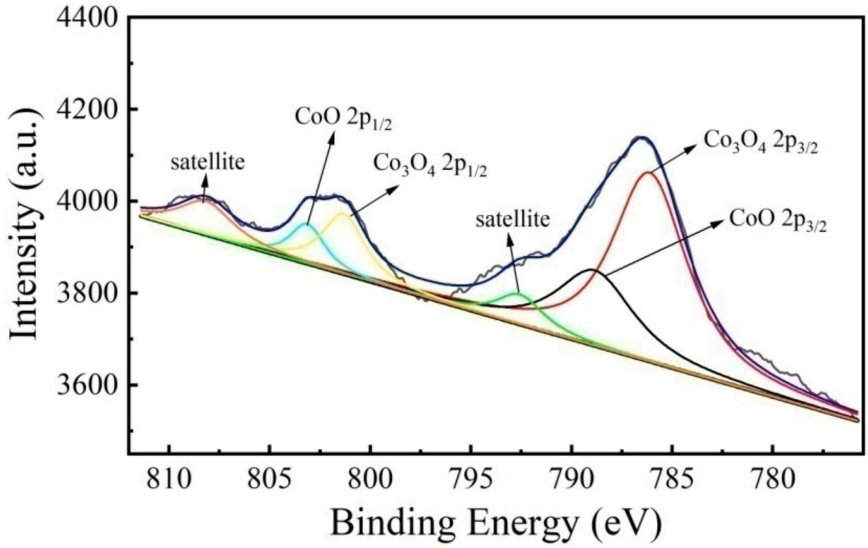


**Figure 3.** Co2p XPS spectra of unsupported $Co/MSiO_2$ material with $n_{Co}$ = 0.08 calcined at 400 °C under $N_2$ atmosphere.

### *3.2. FTIR Analysis*

To further consider the influence of $n_{Co}$ on chemical structure for the unsupported $Co/MSiO_2$ materials, the unsupported $Co/MSiO_2$ materials with various $n_{Co}$ calcined in $N_2$ atmosphere at 400 °C are characterized by FTIR spectra, which are shown in Figure 4. In Figure 4, the peak appearing at about 2978 $cm^{-1}$ is attributed to the $–CH_3$ groups for TEOS and MTES. The absorption peak located at 1640 $cm^{-1}$ is associated with the stretching and bending vibration of –OH groups [42] from the absorbed water and ethanol as well as Si–OH. Undoubtedly, the existence of 1276 $cm^{-1}$ band indicates the stretching vibration of the $Si–CH_3$ groups. The band located at 770–800 $cm^{-1}$ is accompanied by a shoulder, which is attributed to the asymmetric tensile vibration of the Si–O–Si bonds [43]. For $Co/MSiO_2$ material with $n_{Co}$ = 0, the absorption peak at about 1055 $cm^{-1}$ is also assigned to the vibration of Si–O–Si bonds. With the increasing $n_{Co}$, the Si–O–Si bonds centered at 1055 $cm^{-1}$ gradually shift to a lower value. The movement of Si–O–Si bonds indicates that Co enters the $SiO_2$ lattice and that Si–O–Co bonds exist in the materials, which destroys the symmetry of $SiO_2$ and causes the move of peak position. A similar phenomenon has been reported in other literature [44,45]. In addition, when $n_{Co}$ = 0.5, an additional peak is found located at 960 $cm^{-1}$ and corresponding to the Si–O–Co vibration, suggesting that cobalt enters into the silica framework and forms the Si–O–Co bonds. However, Si–O–Co bonds in the samples with $n_{Co}$ = 0.08 and 0.15 are not obvious, which may be owing to the fact that the Si–O–Co bonds cannot be detected when the content of doped cobalt is small. Generally, the FTIR bands assigned to $Co_3O_4$ are located at 571 $cm^{-1}$ and 664 $cm^{-1}$ [46], but there is no obvious peak of $Co_3O_4$ in this figure, which does not imply that $Co_3O_4$ is not present in the samples. The reason may be that the content of $Co_3O_4$ is too small, and the peak is not revealed.

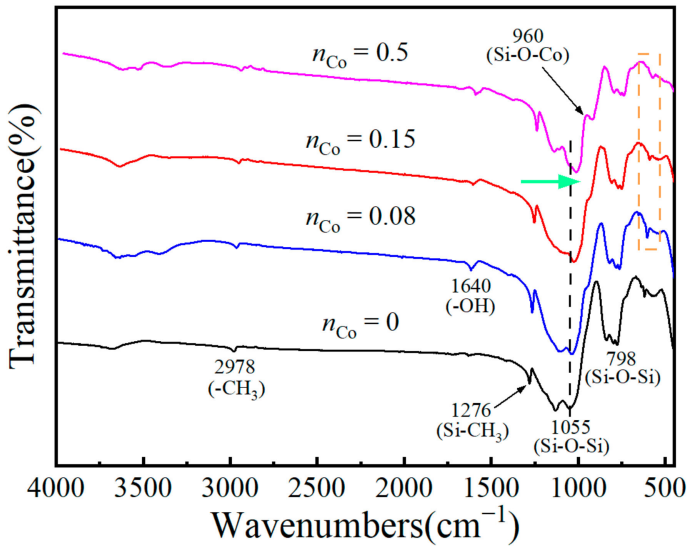


**Figure 4.** FTIR spectra curves of unsupported Co/$MSiO_2$ materials with various $n_{Co}$ calcined in $N_2$ atmosphere at 400 °C (the green arrow represents the direction in which the Si−O−Si bonds centered at 1055 cm$^{-1}$ moves; the dotted rectangle emphasizes the peaks at 571 and 664 cm$^{-1}$).

### *3.3. Pore-Structure Analysis*

The physical characteristics of the prepared samples can be greatly influenced by their specific surface area and porous structure. The $N_2$ adsorption-desorption isotherm curves of unsupported Co/$MSiO_2$ materials with various $n_{Co}$ at 400 °C are displayed in Figure 5a. As shown in Figure 5a, the isotherms for the four samples all show a similar trend, which can be categorized as type I isotherm. In the range of low relative pressure $P/P_0 < 0.1$, a substantial amount of adsorption indicates that there is a giant quantity of micropores in the materials. As the relative pressure increases, the isotherm gradually increases, which confirms the existence of a small amount of mesopores. The $N_2$ adsorption of unsupported Co/$MSiO_2$ materials increases initially with the increasing $n_{Co}$, then begins to decrease as $n_{Co} > 0.08$, which indicates the change of pore-volume variation trend. The distributions of pore size for all samples are depicted in Figure 5b. It is found that the unsupported Co/$MSiO_2$ materials with $n_{Co}$ = 0.08–0.5 have a wider pore size distribution and a bigger mean pore size than the sample with $n_{Co}$ = 0. In addition, the pore diameters of all samples are mainly concentrated around 1.3 nm. The detailed information about the pore size and surface area for these four samples is provided in Table 1. It can be observed that, with the increases of $n_{Co}$, the mean pore size increases, and the micropore volume decreases; the total pore volume and BET surface area increase until $n_{Co}$ = 0.08, after which they begin to decrease. This is because the added cobalt atoms exist in the form of Si–O–Co bonds in the $SiO_2$ skeleton, and the atomic radius of the cobalt atoms is larger than that of the silicon atoms, which plays a role in expanding the pores [45]. So, with the increase of $n_{Co}$, the particle size, mean pore size, total pore volume, and surface area, the distribution of pore size becomes wider and shifts gradually to the direction of the mesopores. However, as $n_{Co} > 0.08$, in addition to the existence of cobalt in the skeleton in the amorphous form, there are also some cobalt oxides interspersed in the pores to block part of the pores, which leads to a decreasing in the pore volume and BET surface area. When $n_{Co}$ = 0.08, the unsupported Co/$MSiO_2$ material is more favorable for achieving a higher total pore volume (0.424 cm$^3$·g$^{-1}$) and BET surface area (775.344 m$^2$·g$^{-1}$), with the minimum mean pore diameter (2.34 nm). Therefore, the unsupported Co/$MSiO_2$ material with $n_{Co}$ = 0.08 is more favorable for gas separation.

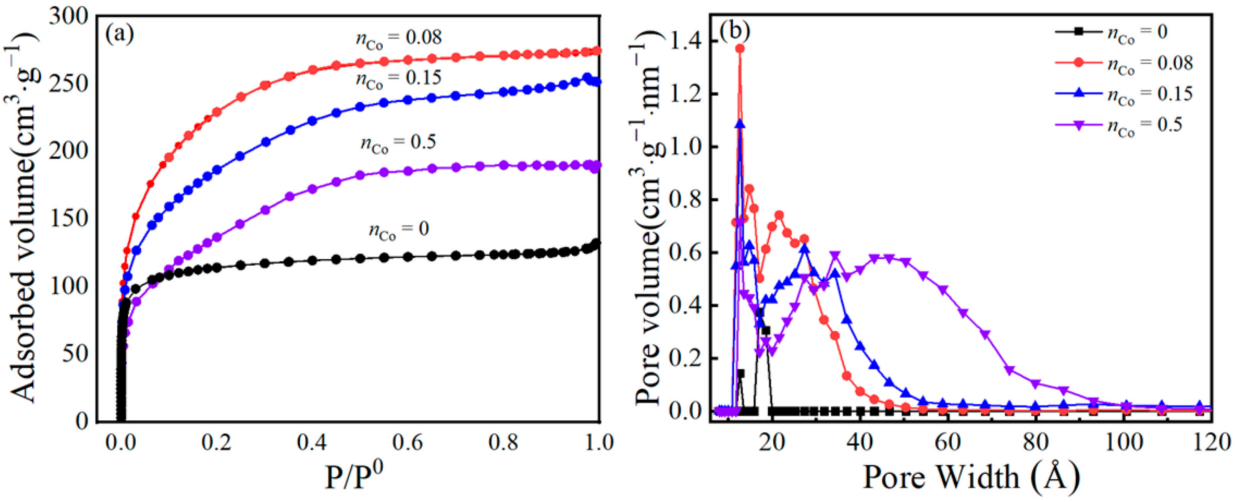


**Figure 5.** (**a**) $N_2$ adsorption-desorption isotherms and (**b**) pore size distributions of unsupported $Co/MSiO_2$ materials with various $n_{Co}$ at 400 °C.

**Table 1.** Parameters of pore structure for unsupported $Co/MSiO_2$ materials with various $n_{Co}$ after calcination at 400 °C.

| Membrane Materials | BET Surface Area ($m^2$/g) | Total Pore Volume ($cm^3$/g) | Micropore Volume ($cm^3$/g) | $V_M/V_t$ | Mean Pore Size (nm) |
|---|---|---|---|---|---|
| $n_{Co}$ = 0 | 389.38 | 0.230 | 0.150 | 0.652 | 1.75 |
| $n_{Co}$ = 0.08 | 775.34 | 0.424 | 0.045 | 0.106 | 2.34 |
| $n_{Co}$ = 0.15 | 644.10 | 0.402 | 0.035 | 0.087 | 2.73 |
| $n_{Co}$ = 0.5 | 494.54 | 0.399 | 0.034 | 0.085 | 3.14 |

### *3.4. TEM Analysis*

To gain an insight into the Co species, the TEM analysis was performed to determine the presence of Co species in unsupported $Co/MSiO_2$ materials with various $n_{Co}$ calcined in $N_2$ atmosphere at 400 °C. Figure 6 demonstrates the transmission electron microscope images for unsupported $Co/MSiO_2$ materials with $n_{Co}$ = 0, 0.08, and 0.15 calcined in $N_2$ atmosphere at 400 °C. For these three samples, because of differences in electronic density, the darker-contrast particles can be attributed to cobalt oxide, while the lighter-contrast particles are attributed to silica carrier. In Figure 6a, amorphous silica can be observed on $Co/MSiO_2$ material with $n_{Co}$ = 0. In Figure 6b,c, a small amount of the CoO crystals are uniformly dispersed on the surface of $Co/MSiO_2$ materials with $n_{Co}$ = 0.08 and 0.15, and the particle size of the CoO crystals increases with the increasing $n_{Co}$. Furthermore, the crystal size of CoO in $Co/MSiO_2$ material with $n_{Co}$ = 0.08 is in the range of 1.3–2.2 nm, and that in the $Co/MSiO_2$ material with $n_{Co}$ = 0.15 is in the range of 1.9–2.7 nm. Nevertheless, no $Co_3O_4$ particles were found on the outside surfaces of two samples, which does not imply that $Co_3O_4$ does not exist in the samples. This may be due to the tiny amount. For the unsupported $Co/MSiO_2$ material with $n_{Co}$ = 0.5, it is clear that particles of $Co_3O_4$ and CoO are scattered on the surface of the sample by TEM analysis because of a higher Co content. Thus, the sample is not introduced here. It can be seen that the conclusions obtained above are consistent with the results from the XRD and XPS analysis.

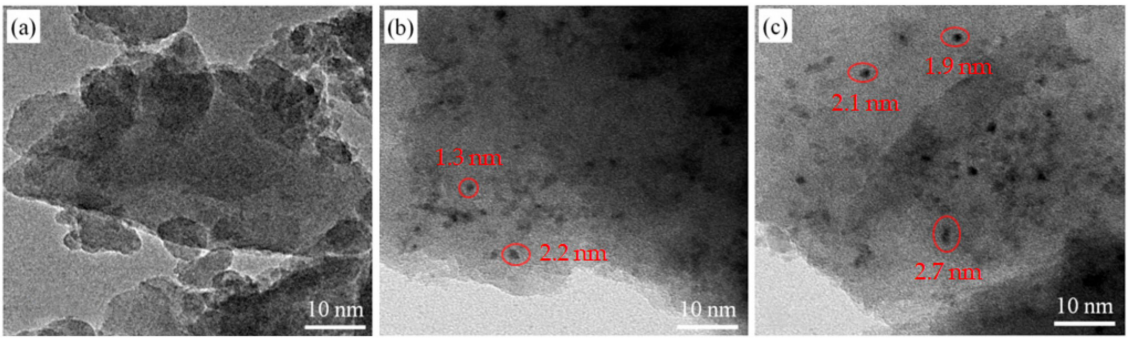


**Figure 6.** TEM images of unsupported $Co/MSiO_2$ materials with $n_{Co}$ = (**a**) 0, (**b**) 0.08, and (**c**) 0.15 calcined in $N_2$ atmosphere at 400 °C.

### *3.5. Gas-Permeance Analysis*

Based on the XRD, XPS, FTIR, $N_2$ adsorption-desorption, and TEM results, the $n_{Co}$ shows obvious impact on the physical-chemical structures of unsupported $Co/MSiO_2$ materials. However, compared with the unsupported $Co/MSiO_2$ materials with $n_{Co}$ = 0.08 and 0.15, the pore volume and surface area for unsupported $Co/MSiO_2$ materials with $n_{Co}$ = 0.5 are smaller, whereas the mean pore size is larger. As far as we know, the permeation and selectivity of gas-separation membrane are dependent on the pore structure and surface area. It could suggest that the supported $Co/MSiO_2$ membrane with $n_{Co}$ = 0.5 is not suitable for gas-permeation experiments. Therefore, the supported $Co/MSiO_2$ membrane with $n_{Co}$ = 0.5 is not considered here. The permeances for gases ($H_2$, $CO_2$, and $N_2$) to the gas molecules' kinetic diameters ($d_k$) and $H_2$ perm-selectivities of $Co/MSiO_2$ membrane with $n_{Co}$ = 0, 0.08, and 0.15 at a pressure difference of 0.2 MPa and 200 °C are shown in Figure 7. The gas molecules' kinetic diameters can be acquired from the report in [47]. The $Co/MSiO_2$ membrane with $n_{Co}$ = 0 is also referred to as $MSiO_2$ membrane. From Figure 7a, as $n_{Co}$ > 0.08, the permeances of $Co/MSiO_2$ membrane to $H_2$, $CO_2$, and $N_2$ appears to decrease. The $H_2$ permeance of $Co/MSiO_2$ membranes with $n_{Co}$ = 0, 0.08, and 0.15 are $9.07 \times 10^{-6}$, $1.97 \times 10^{-5}$, and $1.41 \times 10^{-5}$ $mol \cdot m^{-2} \cdot Pa^{-1} \cdot s^{-1}$, respectively. Compared with the $Co/MSiO_2$ membrane with $n_{Co}$ = 0, the $H_2$, $CO_2$, and $N_2$ permeances of $Co/MSiO_2$ membrane with $n_{Co}$ = 0.08 increase by 1.17, 0.70, and 0.83 times, respectively. It can be seen from the pore structure analysis that the total pore volume and average pore diameters for the silica membranes enlarge slightly with increasing $n_{Co}$, giving an explanation for the increase in gas permeance. Furthermore, for the same membrane, the order for permeance of gas molecules is $N_2 < CO_2 < H_2$. The gas permeation decreases as the $d_k$ increases, suggesting that all membranes show molecular sieve characteristics. These above results indicate that the porosity of the membrane shows a mean pore size of approximately 0.3 nm. It can be observed from Figure 7b that the perm-selectivities of $H_2/CO_2$ and $H_2/N_2$ for $Co/MSiO_2$ membranes with various $n_{Co}$ are all significantly higher than the ideal perm-selectivities of Knudsen diffusion, which are 4.69 and 3.74, respectively. Compared with $MSiO_2$ membrane, the $H_2/CO_2$ and $H_2/N_2$ perm-selectivities of $Co/MSiO_2$ membrane with $n_{Co}$ = 0.08 increase by 27.66% and 18.53%, respectively. Therefore, the amplification of $H_2$ perm-selectivities is not entirely ruled by the aid of molecular sieving; however, it may additionally be partly attributed to the improved adsorption of hydrogen by means of the $Co/MSiO_2$ membrane matrix. The consequences of improved $H_2$ perm-selectivities have additionally been mentioned for the $Ni/SiO_2$ [20] and $Pd/SiO_2$ [24] membranes, which have been ascribed to the enlarge affinity of $H_2$ with the aid of the metallic particles. Moreover, when $n_{Co}$ = 0.08, the $H_2$ perm-selectivities of the $Co/MSiO_2$ membrane reach the maximum value. However, as the $n_{Co}$ continues to increase, the $H_2$ perm-selectivities show a gradual decrease. The above consequences point out that the $n_{Co}$ performs an advantageous function in the impact of gas permeation for the membrane, but it does not mean that the higher the $n_{Co}$, the better the gas-permeation

effect. Thus, the Co/$MSiO_2$ membrane with $n_{Co}$ = 0.08 has good gas permeability and selectivity, which is more appropriate for gas-permeation experiments.

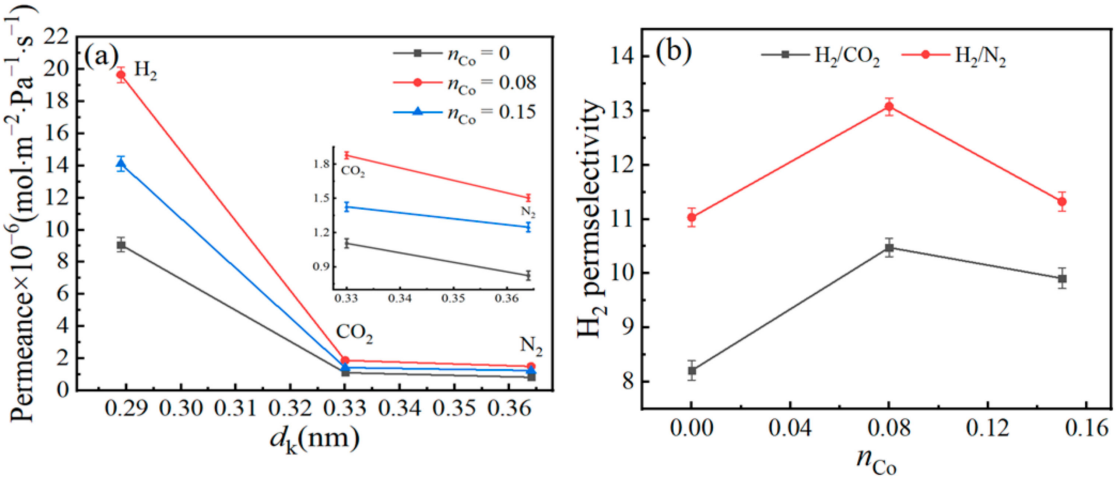


**Figure 7.** (**a**) Gases' ($H_2$, $CO_2$, and $N_2$) permeances versus gas molecules' kinetic diameters ($d_k$) and (**b**) $H_2$ perm-selectivities of supported Co/$MSiO_2$ membranes with various $n_{Co}$ at a pressure difference of 0.2 MPa and 200 °C.

Figure 8 displays the influence for pressure difference on the gases' ($H_2$, $CO_2$, and $N_2$) permeances of $MSiO_2$ membrane at 200 °C; their pressure difference is generally unbiased, whilst that for $H_2$ in Co/$MSiO_2$ membrane with $n_{Co}$ = 0.08 increases significantly with growing pressure difference. It suggests that, due to the impact of the incorporated metal cobalt, the mechanism of $H_2$ diffusion for Co/$MSiO_2$ membrane is different from that for $MSiO_2$ membrane. There are small mesopores on the membrane surface, which leads to the result that the obtained Co/$MSiO_2$ membranes are accompanied by Knudsen diffusion. However, the doped metallic cobalt can improve the surface diffusion of $H_2$ molecules in $SiO_2$ membranes, and the growth of pressure is conducive to the adsorption of hydrogen. In addition, with the gradual increase of pressure, slight increases in the permeances of $CO_2$ and $N_2$ for Co/$MSiO_2$ membrane are observed, which is due to the small influence of pressure on Knudsen diffusion, as previously reported in other literature [48,49]. Accordingly, the permeances of $CO_2$ and $N_2$ in Co/$MSiO_2$ membrane are slightly dependent on pressure, whereas the $H_2$ permeance increases within the pressure range due to the enhanced surface diffusion of hydrogen molecules by the cobalt particles.

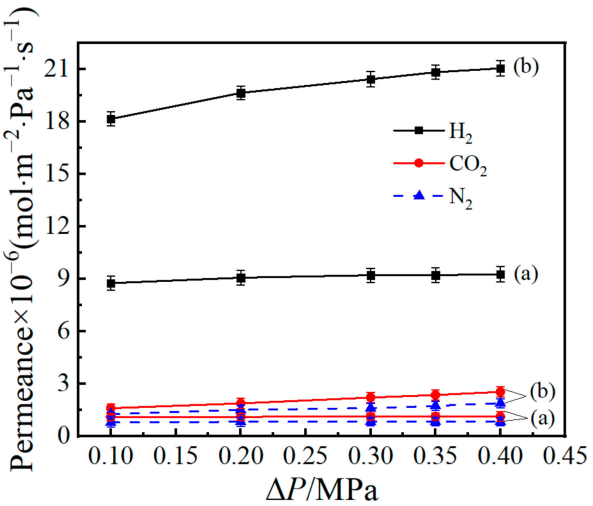


**Figure 8.** Influence of pressure difference on the gases' ($H_2$, $CO_2$, and $N_2$) permeances for supported (**a**) $MSiO_2$ membrane and (**b**) supported Co/$MSiO_2$ membrane with $n_{Co}$ = 0.08 at 200 °C.

The temperature dependence of the various gases' ($H_2$, $CO_2$, and $N_2$) permeances and $H_2/CO_2$ perm-selectivities in the $MSiO_2$ membrane and $Co/MSiO_2$ membrane with $n_{Co}$ = 0.08 at a pressure difference of 0.2 MPa are further investigated in the temperature range of 25–200 °C, which is depicted in Figure 9. In Figure 9a, with the continuous increase of temperature, the $H_2$ permeance in $MSiO_2$ and $Co/MSiO_2$ membranes gradually increases, indicating that the permeation behavior of $H_2$ in the two membranes mainly follows the activation-diffusion mechanism. In contrast, the permeances of $CO_2$ and $N_2$ are slightly decreased in a similar tendency to Knudsen diffusion in which molecules collide with pore walls more regularly than permeating molecules. In the case of activated diffusion, molecules permeate via micropores whilst being uncovered to repelling forces from the pore walls, and molecules with sufficient kinetic energy to conquer the repulsive force can permeate into the pores [38]. The decreasing permeances of $CO_2$ and $N_2$ are attributed to the violent movement of molecules and the increase of the mean free path when the temperature increases. As shown in Figure 9b, as temperature continues to increase in this range, the $H_2/CO_2$ and $H_2/N_2$ perm-selectivities for $MSiO_2$ and $Co/MSiO_2$ membranes all show a gradual, increasing trend. Compared with $MSiO_2$ membrane, when operated at 25 °C, the permeance of $H_2$, and the perm-selectivities of $H_2/CO_2$ and $H_2/N_2$ for $Co/MSiO_2$ membrane increase by 121.53%, 22.76%, and 16.50%, respectively; on the other hand, when operated at 200 °C, those increase by 116.73%, 27.66%, and 18.53%, respectively. In addition, it can be found that, in the temperature range of 25–200 °C, the perm-selectivities of $H_2/CO_2$ and $H_2/N_2$ in both membranes are greater than the ideal perm-selectivities of Knudsen diffusion (4.69 and 3.74). The above results show that the $Co/MSiO_2$ membrane has better perm-selectivity and permeance of $H_2$ than those of $MSiO_2$ membrane under same conditions.

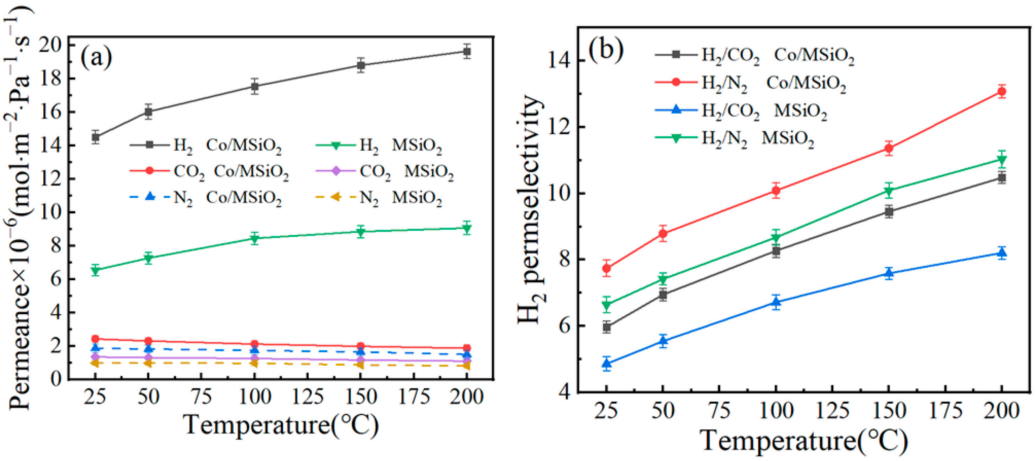


**Figure 9.** Influence of temperature on the (**a**) gases' ($H_2$, $CO_2$, and $N_2$) permeances and (**b**) $H_2$ perm-selectivities for supported $MSiO_2$ membrane and supported $Co/MSiO_2$ membrane with $n_{Co}$ = 0.08 at 0.2 MPa.

The apparent activation energy ($E_a$) is an index of the probability of molecules passing through shrinkage, so lower activation energy is related to higher permeability. According to the Arrhenius equation [16,38], permeability $F$ is a temperature-related parameter, which can be expressed by modified Fick's law:

$$F = \exp\left(-\frac{E_a}{RT}\right) \quad (2)$$

where $F$ is the gas permeability, $E_a$ is the apparent permeation-activation energy, $F_0$ is a temperature-independent parameter, $R$ is the constant of gas and $T$ is the temperature of gas, and the unit is K. Equation (2) can be described in another form:

$$\ln F = \ln F_0 - \frac{E_a}{RT} \quad (3)$$

In order to further study the diffusion phenomenon of gas molecules through $MSiO_2$ and $Co/MSiO_2$ membrane, the Arrhenius diagram is established, and the $E_a$ values of gases' ($H_2$, $CO_2$, and $N_2$) permeations in $MSiO_2$ and $Co/MSiO_2$ film are calculated by using Arrhenius relationship between natural logarithm of permeation and reciprocal of temperature; the corresponding results are plotted in Figure 10. The $E_a$ values of gases ($H_2$, $CO_2$, and $N_2$) can be calculated from the Arrhenius formula for $MSiO_2$ membrane and $Co/MSiO_2$ membrane with $n_{Co}$ = 0.08 at 0.2 MPa, which are listed in Table 2. It can be observed from Table 2 that the $E_a$ value of $H_2$ is positive, while the $E_a$ values of $CO_2$ and $N_2$ are negative, which are conclusions that resemble those of previous reports [50]. The positive or negative value of $E_a$ is related to the activated transportation behavior. The activation energy indicates the repulsive energy of osmotic substance passing through the pore structure of membrane [51]. Gas transport in the microporous state is carried out by heat-activated surface-diffusion mechanism [27]. The negative values $E_a$ of $CO_2$ and $N_2$ indicate that there is a percolation path in the membrane, which is ample enough to enable the diffusion of larger molecules. The $E_a$ values of gases ($H_2$, $CO_2$, and $N_2$) in the $Co/MSiO_2$ membrane are less than those in the $MSiO_2$ membrane, which indicates that the structure of the $Co/MSiO_2$ membrane is more open than that of the $MSiO_2$ membrane, and the above observations are very consistent with the results of $N_2$ adsorption-desorption. This result also suggests that the doping of cobalt successfully reduces the densification of $SiO_2$ network. The larger porosity of $Co/MSiO_2$ membrane leads to the kinetic energy of gas molecules overcoming the membrane pore barrier since it is less than that of $MSiO_2$ membrane. Therefore, the gases' ($H_2$, $CO_2$, and $N_2$) permeances of $Co/MSiO_2$ membrane are greater than those of $MSiO_2$ membrane.

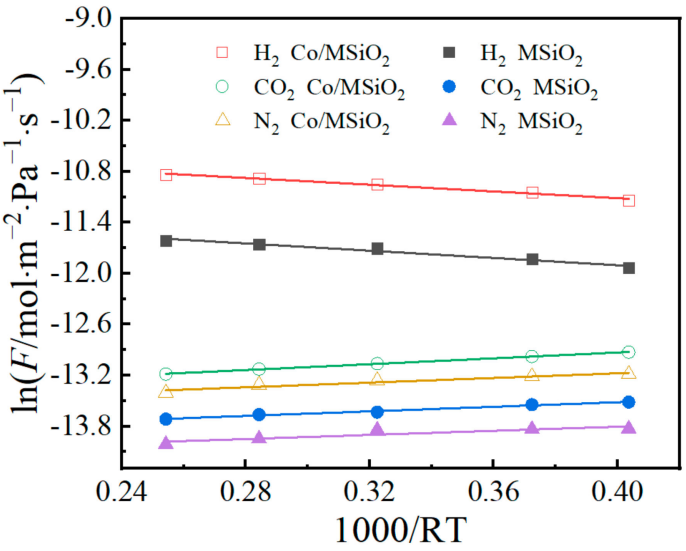


**Figure 10.** Arrhenius plots of gases' ($H_2$, $CO_2$, and $N_2$) permeances in supported $MSiO_2$ membrane and supported $Co/MSiO_2$ membrane with $n_{Co}$ = 0.08 at 0.2 MPa.

**Table 2.** $E_a$ values of gases ($H_2$, $CO_2$, and $N_2$) calculated from Arrhenius formula for supported $MSiO_2$ membrane and supported $Co/MSiO_2$ membrane with $n_{Co}$ = 0.08 at 0.2 MPa.

| Gases | $E_a$/KJ·mol$^{-1}$ | |
|---|---|---|
| | **$MSiO_2$** | **$Co/MSiO_2$** |
| $H_2$ | 2.14 | 1.98 |
| $CO_2$ | −1.34 | −1.72 |
| $N_2$ | −1.21 | −1.37 |

Table 3 shows perm-selectivities of $H_2$, permeances of $H_2$, $E_a$ values of $H_2$, and pore diameters for various $SiO_2$ membranes prepared by other researchers using sol-gel process. As can be viewed from Table 3, it is hard to enhance the perm-selectivity and permeance of gas for the $SiO_2$ membranes at the same time. Generally, larger average pore diameter leads to higher permeance of $H_2$, lower perm-selectivity of $H_2$, and smaller $E_a$ value of $H_2$. Besides, the $E_a$ value of $H_2$ has a link with the interplay between the molecules of $H_2$ and the pore walls of the membrane. Therefore, probably due to the fact that the average pore diameters of the prepared $Co/MSiO_2$ membranes are larger than that of the membrane obtained by different researchers listed in Table 3, it leads to smaller $E_a$ values of $H_2$ and higher permeance of $H_2$. Due to the drawbacks for the conditions of experiment and technology, the perm-selectivities of $H_2$ for the prepared $Co/MSiO_2$ membrane is insufficient to reach significant value.

**Table 3.** Perm-selectivities of $H_2$, permeances of $H_2$, $E_a$ value of $H_2$, and pore diameter for various $SiO_2$ membranes prepared by other researchers using sol-gel process.

| Membrane Type | Temperature and Pressure | Permeance of $H_2$ (mol·m$^{-2}$·Pa$^{-1}$·s$^{-1}$) | Perm-Selectivities of $H_2$ | | Calcination Atmosphere | $E_a$ Value of $H_2$ (KJ·mol$^{-1}$) | Pore Diameter (nm) |
|---|---|---|---|---|---|---|---|
| | | | $H_2/CO_2$ | $H_2/N_2$ | | | |
| Si(400) [49] | 200 °C, 1 bar | $1.74 \times 10^{-6}$ | 7.5 | 64.4 | Air | 8 | 0.38–0.55 |
| $SiO_2$ [52] | 200 °C, 2 bar | $4.62 \times 10^{-7}$ | 3.7 | 10.5 | $N_2$ | — | 0.30–0.54 |
| $SiO_2$–$ZrO_2$ [53] | 500 °C, 100 KPa | $2 \times 10^{-6}$ | 15 | 190 | Air | 13 | — |
| $Pd/SiO_2$ [25] | 200 °C, 0.3 MPa | $7.26 \times 10^{-7}$ | 4.3 | 14 | $H_2$, $N_2$ | — | ~0.57 |
| $Nb/SiO_2$ [54] | 200 °C, 2 bar | $5.03 \times 10^{-7}$ | 3.5 | 6.5 | $N_2$ | — | ~0.55 |
| $Co/SiO_2$ [50] | 200 °C, 500 KPa | $5 \times 10^{-8}$ | 31.6 | — | Air | 13.8 | — |
| $Co/SiO_2$ * | 200 °C, 0.2 MPa | $1.97 \times 10^{-5}$ | 10.48 | 13.08 | $N_2$ | 1.98 | 0.3–2.3 |

* In this work.

The transport of $H_2$, $CO_2$, and $N_2$ in $MSiO_2$ membrane is controlled by molecular sieving, but Knudsen diffusion still exists due to the presence of small mesopores. However, thanks to the absorption for molecules of $H_2$ by cobalt, the introduction of cobalt particles improves the surface diffusion of molecules of $H_2$ in $SiO_2$ membranes, which promotes the transmission of $H_2$ and leads to the growth for permeance of $H_2$ in the $Co/MSiO_2$ membrane. Hence, we can find that, compared with $CO_2$ and $N_2$, the $Co/MSiO_2$ membrane has the higher permeation rate to $H_2$. Consequently, compared with $MSiO_2$ membrane, the permeance of $H_2$ and the perm-selectivities of $H_2/CO_2$ and $H_2/N_2$ in $Co/MSiO_2$ membrane increase simultaneously. The possible change mechanism of $MSiO_2$ and $Co/MSiO_2$ membranes for separating $H_2/CO_2$ is schematically illustrated in Figure 11.

In order to look into the stability for $MSiO_2$ membrane and $Co/MSiO_2$ membrane with $n_{Co}$ = 0.08 under hydrothermal conditions, they were subjected to saturated steam at 200 °C for 10 days and then regenerated by calcination at 350 °C. Figure 12 compares the effects of hydrothermal conditions on the both membrane samples. The experimental data were obtained at a pressure difference of 0.2 MPa and 200 °C. After steam treatment, the permeances of $H_2$, $CO_2$, and $N_2$ for $MSiO_2$ and $Co/MSiO_2$ membranes appear to decrease. Compared with the untreated fresh samples, the permeance of $H_2$ for $MSiO_2$ and $Co/MSiO_2$ membranes after steam aging for 10 days decrease by 21.06% and 7.48%, respectively, and the perm-selectivities of $H_2/CO_2$ and $H_2/N_2$ for $MSiO_2$ membrane decrease by 4.13% and 3.54%, respectively, whereas those of $Co/MSiO_2$ membrane increase by 3.37%

and 2.55%, respectively. After regeneration by calcination at 350 °C, the permeances of gases ($H_2$, $CO_2$, and $N_2$), the perm-selectivities $H_2/CO_2$ and $H_2/N_2$ for two membranes show an upward trend. However, compared with those of the untreated fresh samples, the permeances of $H_2$ for $MSiO_2$ and $Co/MSiO_2$ membranes after regeneration decrease by 11.25% and 4.15%, respectively, whereas the perm-selectivities of $H_2/CO_2$ and $H_2/N_2$ for $MSiO_2$ membrane increase by 5.80% and 4.64%, respectively, and those for $Co/MSiO_2$ membrane increase by 5.03% and 3.49%, respectively. These results mightily indicate that regeneration causes structural changes of $SiO_2$ membrane. The reduction of permeation for two membranes indicates that pore shrinkage of the membrane occurs after regeneration by calcination at 350 °C. The obtained smaller pores result in a lower permeance and higher perm-selectivity. However, a smaller decrease in permeation of $H_2$ for $Co/MSiO_2$ membrane indicates that the diffusion of hydrogen through the surface of cobalt particles could dominate permeation of $H_2$. Therefore, the above results indicate that the $Co/MSiO_2$ membrane has better hydrothermal stability and reproducibility than $MSiO_2$ membrane.

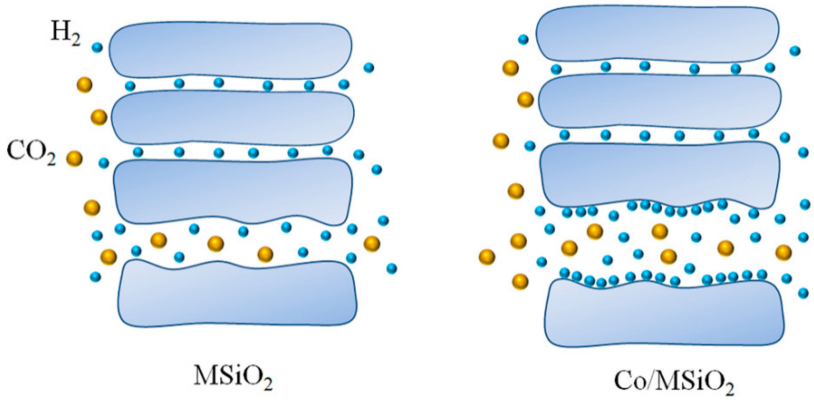


**Figure 11.** A possible schematic diagram for the change mechanism of supported $MSiO_2$ and $Co/MSiO_2$ membranes for separating $H_2/CO_2$.

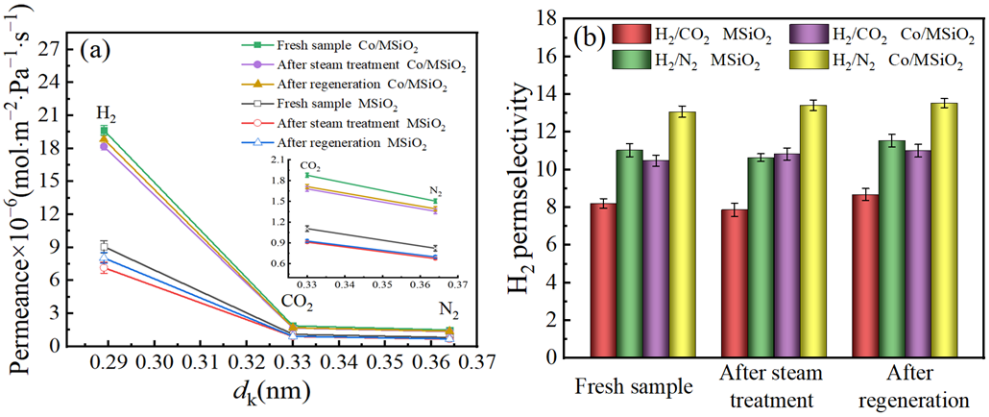


**Figure 12.** Effect of hydrothermal conditions on the (**a**) permeance of $H_2$ and (**b**) perm-selectivities of $H_2$ for supported $MSiO_2$ membrane and supported $Co/MSiO_2$ membrane with $n_{Co}$ = 0.08 at a pressure difference of 0.2 MPa and 200 °C.

### *3.6. SEM Analysis*

The SEM images of membrane surface and cross-sections for $Co/MSiO_2$ membranes with $n_{Co}$ = 0 and 0.08 calcined at 400 °C under $N_2$ atmosphere are shown in Figure 13. In Figure 13a,b, it can be observed that there are no visible cracks and pinholes on $Co/MSiO_2$ membranes surface, indicating that all membranes are well coated. Moreover, the particles on the surfaces of $Co/MSiO_2$ membranes with $n_{Co}$ = 0 are relatively uniform with the particle diameters in the range of 1.2–5.0 nm, while particle diameters of $Co/MSiO_2$ membrane

with $n_{Co}$ = 0.08 are in the range of 1.6–6.3 nm. The cross-section of membrane indicates a classic, uneven configuration, which is related to the morphology of the supported $SiO_2$ membrane. In the cross-section of the SEM image, there is a clear boundary between the support layer and selective layer. The selective layer is found to be smaller for $Co/MSiO_2$ membrane with $n_{Co}$ = 0, with a total thickness about 2.3 μm, whereas the wider selective layer with a total thickness of approximately 2.5 μm can be observed for $Co/MSiO_2$ membrane with $n_{Co}$ = 0.08. In addition, the consequences of gas-permeation measurements show that a complete selective layer has been successfully loaded on the support.

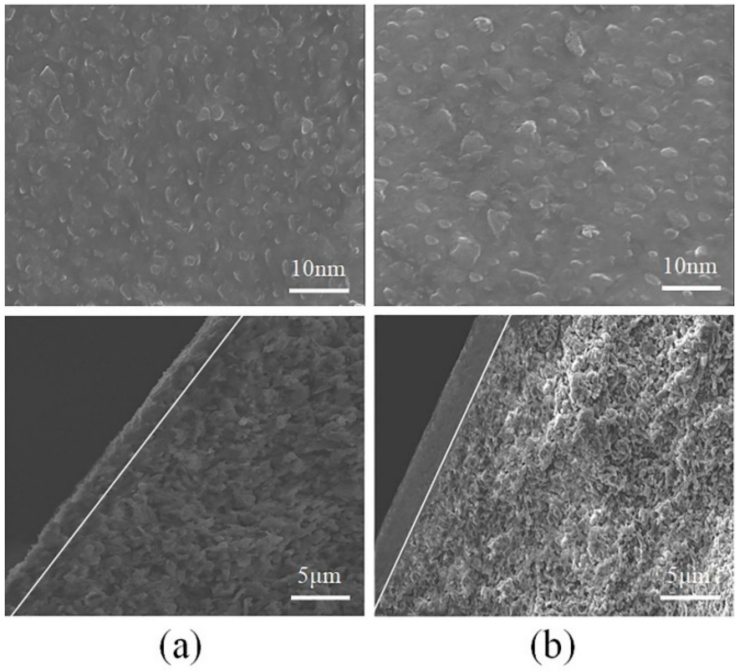


**Figure 13.** SEM images of membrane surface (top images) and cross-sections (bottom images) for supported $Co/MSiO_2$ membranes with $n_{Co}$ = (**a**) 0 and (**b**) 0.08 calcined at 400 °C under $N_2$ atmosphere.

## 4. Conclusions

In summary, $Co/MSiO_2$ materials and membranes with various $n_{Co}$ were successfully synthesized under $N_2$ atmosphere by sol-gel technique. The effect of $n_{Co}$ on the microstructures and perm-selectivities of $H_2$ for $Co/MSiO_2$ membranes were investigated extensively. The results indicate that the cobalt element in $Co/MSiO_2$ material calcined at 400 °C mainly exists in the form of Si–O–Co bond, $Co_3O_4$, and CoO crystals. The $n_{Co}$ has little influence on the thermal stability of $Si–CH_3$ groups of the methyl-modified silica materials. In addition, the introduction of metallic cobalt can enlarge the total pore volume and average pore diameter of the $MSiO_2$ membranes. However, the $n_{Co}$ has a large impact on the gas separation of $Co/MSiO_2$ membrane. When operated at a pressure difference of 0.2 MPa and 200 °C, the $Co/MSiO_2$ membrane with $n_{Co}$ = 0.08 has better gas permeability and selectivity. Compared with $MSiO_2$ membrane, the $H_2$, $CO_2$, and $N_2$ permeances of $Co/MSiO_2$ membrane with $n_{Co}$ = 0.08 increased by 1.17, 0.70, and 0.83 times, respectively, and the perm-selectivities of $H_2/CO_2$ and $H_2/N_2$ increased by 27.66% and 18.53%, respectively. The $E_a$ values of gases ($H_2$, $CO_2$, and $N_2$) in the $Co/MSiO_2$ membrane are less than those in the $MSiO_2$ membrane. After steam treatment, the $H_2$ permeance for $MSiO_2$ and $Co/MSiO_2$ membranes decreased by 21.06% and 7.48%, respectively, and the perm-selectivities of $H_2/CO_2$ and $H_2/N_2$ for $MSiO_2$ membrane decreased by 4.13% and 3.54%, respectively, whereas those of $Co/MSiO_2$ membrane increased by 3.37% and 2.55%, respectively. It is observed that, after regeneration, the permeances of gases ($H_2$, $CO_2$, and $N_2$), the perm-selectivities $H_2/CO_2$ and $H_2/N_2$ for two membranes show an upward trend. However, compared with the untreated fresh samples, the permeances of

$H_2$ for $MSiO_2$ and $Co/MSiO_2$ membranes decreased by 11.25% and 4.15%, respectively, whereas the perm-selectivities of $H_2/CO_2$ and $H_2/N_2$ for $MSiO_2$ membrane increased by 5.80% and 4.64%, respectively, and those for $Co/MSiO_2$ membrane increased by 5.03% and 3.49%, respectively. The $Co/MSiO_2$ membrane has better hydrothermal stability and reproducibility than $MSiO_2$ membrane. In the future, we will further study these separation properties of $Co/MSiO_2$ membranes for mixed gas with water vapor and compare the similarities and differences between the separation of single gas and mixed gas.

**Author Contributions:** Conceptualization, L.W. and J.Y.; methodology, R.M.; formal analysis, Y.G.; writing—original draft preparation, L.W. and J.Y.; project administration, R.M. and H.H.; funding acquisition, L.W., Y.G. and J.Y. All authors have read and agreed to the published version of the manuscript.

**Funding:** This work was supported by the Scientific Research Project of Shaanxi province of China [2021GY-147] and [2021JQ-688], the Scientific Research Project of Shaanxi Education Department, China [No. 19JC017], the Xi'an Municipal Science and Technology Project, China [No. 2020KJRC0025], and Graduate Scientific Innovation Fund for Xi'an Polytechnic University, China [chx2021043].

**Institutional Review Board Statement:** Not applicable.

**Informed Consent Statement:** Not applicable.

**Data Availability Statement:** Not applicable.

**Conflicts of Interest:** The authors declare no conflict of interest.

## References

1. Wang, Y.; Wang, H.; Fu, W.; Yang, X.; Zhang, H.; Huang, Z.; Li, J. Recent Advancement in Heterostructured Catalysts for Hydrogen Evolution Reaction. *J. Mater. Chem. A* **2020**, *8*, 6926–6956. [CrossRef]
2. Chen, W.-H.; Chen, C.-Y. Water gas shift reaction for hydrogen production and carbon dioxide capture: A review. *Appl. Energy* **2019**, *258*, 114078. [CrossRef]
3. Chen, S.; Pei, C.; Gong, J. Insights into Interfacial Catalysis of Steam Reforming Reactions for Hydrogen Production. *Energy Environ. Sci.* **2019**, *12*, 3473–3495. [CrossRef]
4. Ishaq, H.; Dincer, I. Development and multi-objective optimization of a newly proposed industrial heat recovery based cascaded hydrogen and ammonia synthesis system. *Sci. Total Environ.* **2020**, *743*, 140671. [CrossRef]
5. Edwards, P.; Kuznetsov, V.; David, W.I. Hydrogen energy. *Philos. Trans. R. Soc. A Math. Phys. Eng. Sci.* **2007**, *365*, 1043–1056. [CrossRef]
6. Wei, Y.; Zhang, H.; Lei, J.; Song, H.; Qi, H. Controlling pore structures of Pd-doped organosilica membranes by calcination atmosphere for gas separation. *Chin. J. Chem. Eng.* **2019**, *27*, 3036–3042. [CrossRef]
7. Cao, M.; Zhao, L.; Xu, D.; Ciora, R.; Liu PK, T.; Manousiouthakis, V.I.; Tsotsis, T.T. A carbon molecular sieve membrane-based reactive separation process for pre-combustion $CO_2$ capture. *J. Membr. Sci.* **2020**, *605*, 118028. [CrossRef]
8. Tahmasbi, D.; Hossainpour, S.; Babaluo, A.A.; Rezakazemi, M.; Mousavi Nejad Souq, S.S.; Younas, M. Hydrogen separation from synthesis gas using silica membrane: CFD simulation. *Int. J. Hydrogen Energy* **2020**, *45*, 19381–19390. [CrossRef]
9. Ameh, A.E.; Eze, C.P.; Antunes, E.; Cornelius, M.-L.U.; Musyoka, N.M.; Petrik, L.F. Stability of fly ash-based BEA-zeolite in hot liquid phase. *Catal. Today* **2019**, *357*, 416–424. [CrossRef]
10. Prodinger, S.; Derewinski, M.A. Recent Progress to Understand and Improve Zeolite Stability in the Aqueous Medium. *Pet. Chem.* **2020**, *60*, 420–436. [CrossRef]
11. Kim, S.-H.; Park, J.-H.; Hong, Y.; Lee, C.-Y. Removal of BTX using granular octyl-functionalized mesoporous silica nanoparticle. *Int. Biodeterior. Biodegrad.* **2014**, *95*, 219–224. [CrossRef]
12. Araki, S.; Imasaka, S.; Tanaka, S.; Miyake, Y. Pervaporation of organic/water mixtures with hydrophobic silica membranes functionalized by phenyl groups. *J. Membr. Sci.* **2011**, *380*, 41–47. [CrossRef]
13. Messaoud, S.B.; Takagaki, A.; Sugawara, T.; Kikuchi, R.; Oyama, S.T. Alkylamine-silica hybrid membranes for carbon dioxide/methane separation. *J. Membr. Sci.* **2015**, *477*, 161–171. [CrossRef]
14. Kato, H.; Lundin, S.-T.B.; Ahn, S.-J.; Takagaki, A.; Kikuchi, R.; Oyama, S.T. Gas Separation Silica Membranes Prepared by Chemical Vapor Deposition of Methyl-Substituted Silanes. *Membranes* **2019**, *9*, 144. [CrossRef] [PubMed]
15. Han, Y.-J.; Ko, K.-J.; Choi, H.-K.; Moon, J.-H.; Lee, C.-H. Kinetic effects of methane on binary mixture separation on methyltriethoxysilane templated silica membranes. *Sep. Purif. Technol.* **2017**, *182*, 151–159. [CrossRef]
16. Wei, Q.; Ding, Y.-L.; Nie, Z.-R.; Liu, X.-G.; Li, Q.-Y. Wettability, pore structure and performance of perfluorodecyl-modified silica membranes. *J. Membr. Sci.* **2014**, *466*, 114–122. [CrossRef]

17. Ma, X.; Janowska, K.; Boffa, V.; Fabbri, D.; Magnacca, G.; Calza, P.; Yue, Y. Surfactant-Assisted Fabrication of Alumina-Doped Amorphous Silica Nanofiltration Membranes with Enhanced Water Purification Performances. *Nanomaterials* **2019**, *9*, 1368. [CrossRef] [PubMed]
18. Lawal, S.; Kanezashi, M.; Nagasawa, H.; Tsuru, T. Development of an acetylacetonate-modified silica-zirconia composite membrane applicable to gas separation. *J. Membr. Sci.* **2020**, *599*, 117844. [CrossRef]
19. Darmawan, A.; Karlina, L.; Astuti, Y.; Sriatun; Motuzas, J.; Wang, D.; da Costa, J.C.D. Structural evolution of nickel oxide silica sol-gel for the preparation of interlayer-free membranes. *J. Non-Cryst. Solids* **2016**, *447*, 9–15. [CrossRef]
20. Yang, J.; Tian, L. Preparation, Characterization and Surface Free Energy of Nickel-Doped Silica Organic–Inorganic Hybrid Membrane for $H_2/CO_2$ Separation. *J. Nanosci. Nanotechnol.* **2019**, *19*, 3180–3186. [CrossRef]
21. Lee, J.; Ha, J.-H.; Song, I.-H.; Park, J.-W. Facile surface modification of ceramic membranes using binary $TiO_2/SiO_2$ for achieving fouling resistance and photocatalytic degradation. *J. Sol. Gel. Sci. Technol.* **2019**, *91*, 198–207. [CrossRef]
22. Yang, X.; Sheridan, S.; Ding, L.; Wang, D.K.; Smart, S.; Diniz da Costa, J.C.; Liubinas, A.; Duke, M. Inter-layer free cobalt-doped silica membranes for pervaporation of ammonia solutions. *J. Membr. Sci.* **2018**, *553*, 111–116. [CrossRef]
23. Pakdehi, S.G.; Rahimi, E.; Shafiei, K. Effect of Co-$SiO_2$ mesoporous layer coating step on liquid fuel dimethyl amino ethyl azide (DMAZ) dehydration performance. *Chem. Eng. Technol.* **2019**, *42*, 996–1001. [CrossRef]
24. Yang, J.; Fan, W.; Bell, C.-M. Effect of calcination atmosphere on microstructure and $H_2/CO_2$ separation of palladium-doped silica membranes. *Sep. Purif. Technol.* **2019**, *210*, 659–669. [CrossRef]
25. Song, H.; Zhao, S.; Lei, J.; Wang, C.; Qi, H. Pd-doped organosilica membrane with enhanced gas permeability and hydrothermal stability for gas separation. *J. Mater. Sci.* **2016**, *51*, 6275–6286. [CrossRef]
26. Karakiliç, P.; Huiskes, C.; Luiten-Olieman, M.W.J.; Nijmeijer, A.; Winnubst, L. Sol-gel processed magnesium-doped silica membranes with improved $H_2/CO_2$ separation. *J. Membr. Sci.* **2017**, *543*, 195–201. [CrossRef]
27. Boffa, V.; Blank, D.H.A.; Elshof, J.E. Hydrothermal stability of microporous silica and niobia-silica membranes. *J. Membr. Sci.* **2008**, *319*, 256–263. [CrossRef]
28. Ballinger, B.; Motuzas, J.; Smart, S.; da Costa, J.C.D. Palladium cobalt binary doping of molecular sieving silica membranes. *J. Membr. Sci.* **2014**, *451*, 185–191. [CrossRef]
29. Darmawan, A.; Motuzas, J.; Smart, S.; Julbe, A.; da Costa, J.C.D. Binary iron cobalt oxide silica membrane for gas separation. *J. Membr. Sci.* **2015**, *474*, 32–38. [CrossRef]
30. Díez, B.; Roldán, N.; Martín, A.; Sotto, A.; Perdigón-Melón, J.A.; Arsuaga, J.; Rosal, R. Fouling and biofouling resistance of metal-doped mesostructured silica/polyethersulfone ultrafiltration membranes. *J. Membr. Sci.* **2017**, *526*, 252–263. [CrossRef]
31. Battersby, S.; Smart, S.; Ladewig, B.; Liu, S.; Duke, M.C.; Rudolph, V.; da Costa, J.C.D. Hydrothermal stability of cobalt silica membranes in a water gas shift membrane reactor. *Sep. Purif. Technol.* **2009**, *66*, 299–305. [CrossRef]
32. Smart, S.; Vente, J.F.; da Costa, J.C.D. High temperature $H_2/CO_2$ separation using cobalt oxide silica membranes. *Int. J. Hydrog. Energy* **2012**, *37*, 12700–12707. [CrossRef]
33. Liu, L.; Wang, D.K.; Martens, D.L.; Smart, S.; Strounina, E.; da Costa, J.C.D. Physicochemical characterisation and hydrothermal stability investigation of cobalt-incorporated silica xerogels. *RSC Adv.* **2014**, *4*, 18862–18870. [CrossRef]
34. Esposito, S.; Turco, M.; Ramis, G.; Bagnasco, G.; Pernice, P.; Pagliuca, C.; Bevilacqua, M.; Aronne, A. Cobalt-silicon mixed oxide nanocomposites by modified sol-gel method. *J. Solid State Chem.* **2007**, *180*, 3341–3350. [CrossRef]
35. Uhlmann, D.; Liu, S.; Ladewig, B.P.; da Costa, J.C.D. Cobalt-doped silica membranes for gas separation. *J. Membr. Sci.* **2009**, *326*, 316–321. [CrossRef]
36. Ma, H.; Xu, J.; Chen, C.; Zhang, Q.; Ning, J.; Miao, H.; Zhou, L.; Li, X. Catalytic aerobic oxidation of ethylbenzene over Co/SBA-15. *Catal. Lett.* **2007**, *113*, 104–108. [CrossRef]
37. Zhang, W.; Wang, B.; Luo, H.; Jin, F.; Ruan, T.; Wang, D. $MoO_2$ nanobelts modified with an MOF-derived carbon layer for high performance lithium-ion battery anodes. *J. Alloys Compd.* **2019**, *803*, 664–670. [CrossRef]
38. Igi, R.; Yoshioka, T.; Ikuhara, Y.H.; Iwamoto, Y.; Tsuru, T. Characterization of Co-Doped Silica for Improved Hydrothermal Stability and Application to Hydrogen Separation Membranes at High Temperatures. *J. Am. Ceram. Soc.* **2008**, *91*, 2975–2981. [CrossRef]
39. Morad, I.; Liu, X.; Qiu, J. Crystallization-induced valence state change of $Mn^{2+} \rightarrow Mn^{4+}$ in $LiNaGe_4O_9$ glass-ceramics. *J. Am. Ceram. Soc.* **2020**, *103*, 3051–3059. [CrossRef]
40. Riva, R.; Miessner, H.; Vitali, R.; Del Piero, G. Metal–support interaction in $Co/SiO_2$ and $Co/TiO_2$. *Appl. Catal. A Gen.* **2000**, *196*, 111–123. [CrossRef]
41. Lukashuk, L.; Yigit, N.; Li, H.; Bernardi, J.; Föttinger, K.; Rupprechter, G. Operando XAS and NAP-XPS investigation of CO oxidation on meso- and nanoscale CoO catalysts. *Catal. Today* **2019**, *336*, 139–147. [CrossRef]
42. Okoye-Chine, C.G.; Mbuya, C.O.L.; Ntelane, T.S.; Moyo, M.; Hildebrandt, D. The effect of silanol groups on the metal-support interactions in silica-supported cobalt Fischer-Tropsch catalysts. A temperature programmed surface reaction. *J. Catal.* **2020**, *381*, 121–129. [CrossRef]
43. Azmiyawati, C.; Niami, S.S.; Darmawan, A. Synthesis of silica gel from glass waste for adsorption of $Mg^{2+}$, $Cu^{2+}$, and $Ag^{+}$ metal ions. *IOP Conf. Ser. Mater. Sci. Eng.* **2019**, *509*, 1–6. [CrossRef]
44. Zhang, S.; Liu, X.; Shao, Z.; Wang, H.; Sun, Y. Direct $CO_2$ hydrogenation to ethanol over supported $Co_2C$ catalysts: Studies on support effects and mechanism. *J. Catal.* **2020**, *382*, 86–96. [CrossRef]

45. Li, S.; Wang, J.; Ye, Y.; Tang, Y.; Li, X.; Gu, F.; Li, L. Composite Si-O-Metal network catalysts with uneven electron distribution: Enhanced activity and electron transfer for catalytic ozonation of carbamazepine. *Appl. Catal. B* **2020**, *263*, 118311. [CrossRef]
46. Khalil, A.; Ali, N.; Khan, A.; Asiri, A.M.; Kamal, T. Catalytic potential of cobalt oxide and agar nanocomposite hydrogel for the chemical reduction of organic pollutants. *Int. J. Biol. Macromol.* **2020**, *164*, 2922–2930. [CrossRef] [PubMed]
47. Mukherjee, S.; Chen, S.; Bezrukov, A.A.; Mostrom, M.; Terskikh, V.V.; Franz, D.; Wang, S.-Q.; Kumar, A.; Chen, M.; Space, B.; et al. Ultramicropore engineering by dehydration to enable molecular sieving of $H_2$ by calcium trimesate. *Angew. Chem. Int. Ed.* **2020**, *59*, 16188–16194. [CrossRef] [PubMed]
48. He, X.; Hagg, M.-B. Optimization of Carbonization Process for Preparation of High Performance Hollow Fiber Carbon Membranes. *Ind. Eng. Chem. Res.* **2011**, *50*, 8065–8072. [CrossRef]
49. De Vos, R.M.; Verweij, H. Improved performance of silica membranes for gas separation. *J. Membr. Sci.* **1998**, *143*, 37–51. [CrossRef]
50. Liu, L.; Wang, D.K.; Martens, D.L.; Smart, S.; da Costa, J.C.D. Binary gas mixture and hydrothermal stability investigation of cobalt silica membranes. *J. Membr. Sci.* **2015**, *493*, 470–477. [CrossRef]
51. Hacarlioglu, P.; Lee, D.; Gibbs, G.V.; Oyama, S.T. Activation energies for permeation of He and $H_2$ through silica membranes: An ab initio calculation study. *J. Membr. Sci.* **2008**, *313*, 277–283. [CrossRef]
52. Qureshi, H.F.; Nijmeijer, A.; Winnubst, L. Influence of sol–gel process parameters on the micro-structure and performance of hybrid silica membranes. *J. Membr. Sci.* **2013**, *446*, 19–25. [CrossRef]
53. Yoshida, K.; Hirano, Y.; Fujii, H.; Tsuru, T.; Asaeda, M. Hydrothermal Stability and Performance of Silica-Zirconia Membranes for Hydrogen Separation in Hydrothermal Conditions. *J. Chem. Eng. Jpn.* **2001**, *34*, 523–530. [CrossRef]
54. Qureshi, H.F.; Besselink, R.; ten Elshof, J.E.; Nijmeijer, A.; Winnubst, L. Doped microporous hybrid silica membranes for gas separation. *J. Sol Gel Sci. Technol.* **2015**, *75*, 180–188. [CrossRef]